Journal of Cluster Science
https://doi.org/10.1007/s10876-021-02094-5

ORIGINAL PAPER

Zirconium Doped Copper Ferrite ($CuFe_2O_4$) Nanoparticles for the Enhancement of Visible Light-Responsive Photocatalytic Degradation of Rose Bengal and Indigo Carmine Dyes

P. Nancy Dayana[1] · M. John Abel[2] · P. Fermi Hilbert Inbaraj[2] · S. Sivaranjani[3] · R. Thiruneelakandan[1] · J. Joseph prince[2]

Received: 27 February 2021 / Accepted: 17 May 2021
© The Author(s), under exclusive licence to Springer Science+Business Media, LLC, part of Springer Nature 2021

Abstract
In this work, the Zr doped $CuFe_2O_4$ nanoparticles were prepared with different concentrations of zirconium ions through the chemical precipitation method. The Zr ion are added as $Zr_{(x\ wt\%)}$:$CuFe_{2(100\text{-}xwt\%)}O_4$ with (x = 0, 1, 3, 5). The crystal structure and phase were identified by XRD characterization. From the XRD the average crystallite sizes of the synthesized material were calculated and are obtained as 33 nm, 34 nm, 38 nm, and 42 nm. FT-IR characterization was taken to find the functional groups present in the material. The optical properties and corresponding optical band gap were determined by UV-DRS and PL studies. The bandgap was found to be 1.39 eV, 1.56 eV, 1.80 eV, and 1.97 eV for 0%, 1%, 3%, and 5% Zr doped $CuFe_2O_4$ nanoparticles respectively. The surface morphology is studied by SEM analysis. EDAX is used for the elemental composition analysis of the prepared materials. Further, the photocatalytic performances were studied with Rose Bengal (RB) and Indigo Carmine (IC) textile dyes. The maximum degradation percentage was obtained as 88% for RB dye and 71% for IC dye with 5wt% Zr doped $CuFe_2O_4$ nanoparticles within 120 min. The mineralization of the degraded dye solution was confirmed by the Chemical Oxygen Demand (COD) technique.

Keywords Visible light · Zr: $CuFe_2O_4$ · Nanoparticles · Textile dyes · Photocatalyst

Introduction

Water is polluted by the rise in the use of different chemical contaminants in various industries. As a critical source of life, water sources frequently experience the above-mentioned issue as an effect of urbanization and economic development evolve rapidly. Effluent from many factories produces toxic elements that routinely combine with natural water sources. Tapestry, leather, clothing, printing industries, etc. use numerous types of natural and organic dyes to stain their goods, which are very harmful to living things [1–3]. These organic contagious compounds released from certain plants as a dye-waste blend with natural waters pollute aquatic life in the environment as a result of mutagenicity and cancer-causing [4, 5]. Xanthene dyes are one among the numerous dye groups and are widely used as coloring agents in textile industries, dyeing industries and printing and photochemical industries. Rose Bengal is a xanthene dye and these dye groups have been considered to be mutagenic, genotoxic, cytostatic, and cytotoxic [6–10]. Indigo Carmine (IC) is a dye that belongs to the indigoid family that is more poisonous. It is widely used in cosmetics, pharmaceuticals, and food companies. Despite its many applications, IC dye is harmful to humans, causing conjunctivitis and corneal damage, clastogenic activity on bone marrow chromosomes, cause a

✉ R. Thiruneelakandan
rtkchemaut@gmail.com

✉ J. Joseph prince
josephprinceaut@gmail.com

[1] Department of Chemistry, University College of Engineering, Bharathidasan Institute of Technology Campus, Anna University, Tiruchirappalli, Tamil Nadu 620024, India

[2] Department of Physics, University College of Engineering, Bharathidasan Institute of Technology Campus, Anna University, Tiruchirappalli 620024, Tamil Nadu, India

[3] Department of Physics, St.Antony's College of Arts and Sciences for Women, Ammakulathupatti, Tamil Nadu 624005, India

Published online: 02 June 2021

lethal anaphylactic reaction, and severe hemodynamic impact [11–13]. Toxicity and detrimental environmental health consequences are a justification for eliminating these dye wastes from wastewater. Various methods such as adsorption and photocatalysis were utilized to remove these dyes from wastewater. Much study has begun on photocatalysis on semiconductors of metal oxide because of their high stabilization, abundance, and biocompatibility for environmental remediation [14–17]. Photocatalysts are recently recognized as promised products for dye degradation due to various uses, simple operating also operates in moderate environments without special equipment. Photocatalysis is performed by semiconductors on the photon absorption of energy no smaller than the band breach. Electron–hole pairs, electrons in the conductance band (CB) and holes in the valence band (VB) are formed by semiconductors with photon absorption of energy no less than that of the bandgap. Although a fraction of the charge carriers disperse to the surface of the particle and react with the adsorbed dye molecules directly or indirectly, lead to photocatalysis whereas the remaining recombines restricting the photocatalytic ability.

Ferrite nanoparticles are vastly utilized for the mineralization of organic dyes because of their narrow bandgap to active in visible light, catalytic site multiplicity for dye molecule absorption and easy separation after degradation due to their magnetic properties [18, 19]. Due to special properties such as magnetic, electronic, thermal and catalytic properties, copper ferrite ($CuFe_2O_4$) is one of the essential ferrites which have been used in a broad range of applications like gas sensing applications, catalytic treatment, colour mapping, and ferro-fluids. Metal ferrites always have a cubic spinel crystal structure. The General chemical formula of spinel ferrite crystal structure is MFe_2O_4, in which oxygen ions are located at FCC lattice sites, and the metal cations are located in spaces between the oxygen ions. The spinel crystal structure has two different lattice sites one is tetrahedral or A sites and the other is octahedral or B sites. M^{2+} (metal cations) is on A sites, and Fe^{3+} is on B sites in the usual spinel system, but M^{2+} is on B sites, and Fe^{3+} is distributed evenly between A and B sites in the inverse spinel structure. In a random case (mixed spinel), the divalent and trivalent ions usually occupy the B sites [20].

Selective doping of the impurities that recast the band structure by producing quasi-stable energies will help to boost the optoelectronic properties of metal oxides [21]. Hence, various scientists have been involved in the doping of the foreign element to enhance the functional properties of metal oxide NPs. In recent times, numerous doping elements, like Ti, Ce, Zn, Ag, and In were utilized to boost up the functional properties and photocatalytic activity of synthesized $CuFe_2O_4$ NPs [22–26]. Zirconium also has a wide variety of inorganic compounds and coordination complexes, like other transition metals. This compound is usually colourless diamagnetic solids, in which the oxidation state of Zr is 4 + . Zirconium has been tested as an appropriate one for $CuFe_2O_4$ among the various dopants due to the probability of modification of the band gap while maintaining the ionic radius comparable to each other because the ionic radius of Zr^{4+} ions (0.86 Å) is identical to that of Fe^{3+} (0.79 Å). Consequently, in the crystal lattice, Zr^{4+} ions can readily replace Fe^{3+} ions, and the product compound can stabilize the lattice structure. Many reports are available for zirconium used as a doping element with various host materials such as In_2O_3, Ga_2O_3, ZnO, etc. but synthesis and characterization of zirconium doped $CuFe_2O_4$ nanoparticles has not been reported yet. Also, based on our literature review, the photocatalytic activity of nanostructured $CuFe_2O_4$ doped with Zr^{4+} ions was not previously investigated. In connection with the above-mentioned reasons, this work is focused on the synthesis and characterization of Zr doped $CuFe_2O_4$ nanoparticles with three different weight percentages of zirconium through a wet chemical synthesis route. The photocatalytic behavior of the prepared materials was studied by degrading the textile dyes namely Rose Bengal (RB) and Indigo Carmine (IC) under visible light irradiation.

Materials

$Fe(NO_3)_3 \bullet 9H_2O$ (Iron (III) nitrate nonahydrate), $Cu(NO_3)_2 \bullet 6H_2O$ (Copper (II) nitrate hexahydrate), $ZrO(NO_3)_2 \bullet xH_2O$ (Zirconium (IV) oxynitrate hydrate), NH_4OH (25% Aqueous ammonia hydroxide solution), $C_{20}H_2Cl_4I_4Na_2O_5$ (Rose Bengal 95% dye content), and $C_{16}H_8N_2Na_2O_8S_2$ (Indigo Carmine 85% dye content) all these chemicals are brought from Sigma-Aldrich with 99.95% purity and used in the reaction without further purification. (DD) double distilled water is used as a solvent for the reaction.

Method

For synthesizing the copper ferrite ($CuFe_2O_4$) nanoparticles, Iron (III) nitrate nonahydrate and Copper (II) nitrate hexahydrate salts were taken in (0.2 M: 0.1 M) 2:1 ratio and dissolved in 200 ml of DD water. The solution was vigorously stirred for getting a homogenous mixture. Then 20 ml of 25% aqueous ammonia hydroxide solution was added drop by drop into the mixture with continuous and constant stirring. After the completion of the ammonia solution, the whole reaction mixture was kept under constant stirring for 6 h. Then the stirrer is stopped and the beaker containing the reaction mixture was kept

undisturbed for the whole night. Now the precipitate was completely settled at the bottom of the beaker. Then the precipitate was washed with ethanol using filter paper until the pH reaches neutral. The precipitate is then spread over in a petri-dish and kept in a hot air oven for 12 h at 80 °C. Then the dried material was crushed into powder and allowed for calcination at 700 °C up to 3 h in a muffle furnace. The final product was studied using various characterization techniques. For the preparation of Zr doped $CuFe_2O_4$ nanoparticles, 1, 3, 5 wt% of Zirconium (IV) oxynitrate hydrate is added simultaneously into the reaction mixture along with Iron (III) nitrate nonahydrate and Copper (II) nitrate hexahydrate salts by reducing the appropriate amount from Iron (III) nitrate nonahydrate and the remaining procedures are same as mentioned above. For simplification the samples are denoted as S1, S2, S3, and S4 for pure and 1, 3, 5 wt% of Zirconium doped $CuFe_2O_4$ nanoparticles respectively in the rest of the manuscript.

Photocatalytic Test

The photocatalytic experiment was done with two different dyes namely Rose Bengal (RB) and Indigo Carmine (IC). 100 ml of 20 mg/L solutions of two dyes were taken separately and 0.1 g of the photocatalyst was taken as catalyst load. 0.1 g of catalyst from all four samples was taken and mixed separately with each dye solution. Now the dye solutions with catalyst load are stirred gently in order to mix well and kept in dark for 1 h to achieve adsorption/desorption equilibrium between the catalyst and the dye molecules. After that, the dye solutions are transferred to the reactor setup to allow a photocatalytic mechanism. The light was illuminated continuously and the catalyst loaded dye solution was stirred gently and constantly to achieve maximum contact between the catalyst and dye molecules. All These experiments were done with the help of a commercial photo-reactor setup. The reactor consists of a 150 W tungsten halogen lamp for the light source with wavelength ranges from 340 – 850 nm and is mounted between the double-wall borosilicate well with inlet and outlets in which the coolant has been circulated. Here 2 M sodium nitrate ($NaNO_2$) solution was used in order to filter the UV light (320 – 400 nm) emitted by the light source. To analyze the degradation of dye molecules, the aliquots of the dye solution were taken at regular intervals (20 min) and characterized by a UV–Vis spectrophotometer. Also, the percentage of degradation of the dye molecules with respect to time is calculated by the following formula (Eq. 1)

$$\eta = \left(1 - \frac{c}{c_0}\right) \times 100(\%) \tag{1}$$

Results and Discussion

XRD Analysis

The XRD analysis was carried out for confirming the crystal phase and structure of the prepared samples. Figure 1a, reveals the XRD patterns of the prepared samples which is recorded for diffraction angle 2θ ranges from 15 – 80°. From the XRD pattern, it is confirmed that the prepared materials exhibit FCC spinel crystal structure and are well-matched with the standard JCPDS 77–0010 [27]. The lattice parameter values are calculated using the formula (Eq. 2).

$$a = d\sqrt{h^2 + k^2 + l^2} \tag{2}$$

It is found that the lattice parameter increases gradually with the increase in zirconium content (8.3863—8.4125 Å) and is shown in Fig. 1b. This increase is may be due to the Fe^{3+} with a smaller ionic radius (0.79 Å) is replaced by the Zr^{4+} ions having a slightly larger ionic radius (0.86 Å) and also there is a small shift in the predominant peak towards the lower angle of 2θ is noted from the XRD patterns. Hence the XRD pattern confirms the incorporation of Zr^{4+} ions into the $CuFe_2O_4$ crystal lattice. The average crystallite size of all the prepared samples was calculated using the Scherrer formula (Eq. 3).

$$D = \frac{K\lambda}{\beta \cos\theta} \tag{3}$$

The calculated crystallite size is found to be 33 nm, 34 nm, 38 nm, and 42 nm for S1, S2, S3, and S4 nanoparticles respectively. According to the obtained crystallite size, all the synthesized materials are in the nanoscale range. From the XRD analysis, it was found the all the prepared samples have a good degree of crystallinity with a high degree of purity.

FTIR Analysis

The FTIR characterization is taken to identify the various functional groups and their modes of vibrations present in the prepared materials. Figure 2a represents the FTIR spectrum of all the synthesized samples and is recorded from 400 – 4000 cm^{-1}. Usually, the metal oxide vibration modes are obtained between 100 –1000 cm^{-1}. Here two respective transmission peaks were obtained for all the samples. The obtained peak around 470.32 cm^{-1} was due to the vibrational frequency arrived from Cu – O in the

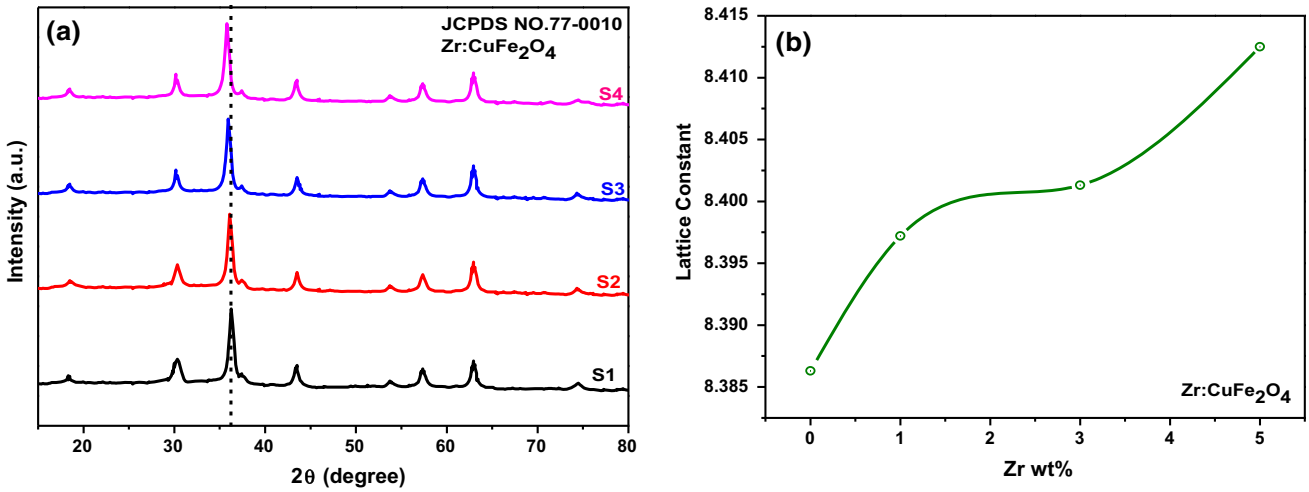

Fig. 1 **a** XRD patterns of the prepared materials **b** Graph between Zr content and lattice parameter

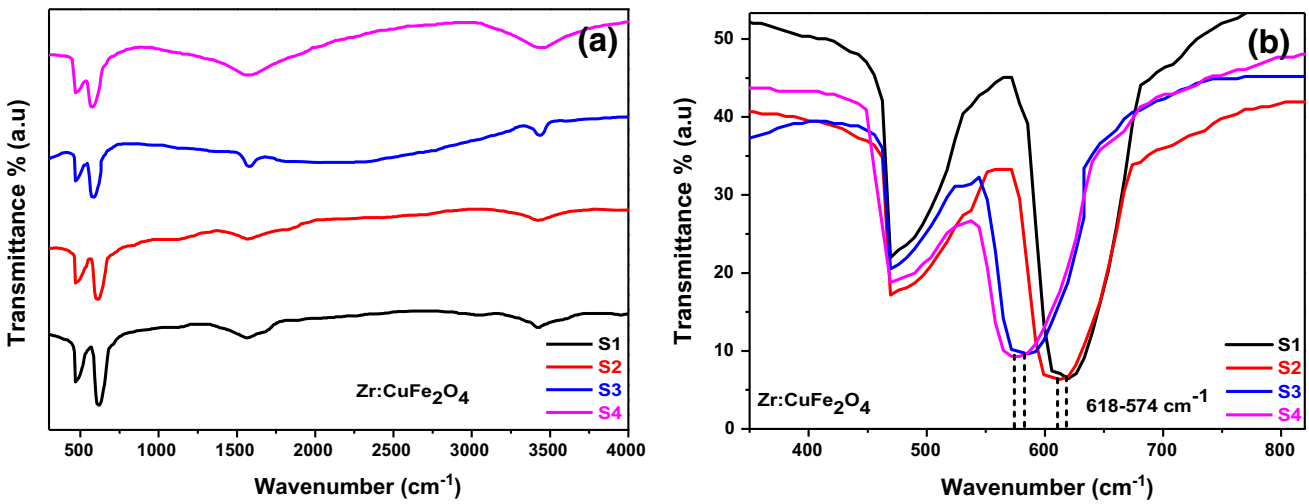

Fig. 2 **a**, **b** FTIR spectra of the materials

tetrahedral sites (A sites) and the transmission peak arrived at the region 574.13 – 618.21 cm^{-1} is due to the Fe – O vibrations in the octahedral sites (B sites) [28]. The peak detected at 3437.43 cm^{-1} is consistent with vibrations there in H–O-H stretching mode. 1579.43 cm^{-1} peak observed in the spectra is due to bending mode vibrations of hydroxyl groups (H–O-H) adsorbed in the sample's surface. Hence the existence of two peaks in the metal oxide region confirms that the prepared samples have a spinel crystal structure and agree with the XRD results. Also, it is found that the peak arrived at the octahedral site is slight shifts towards the lower wavenumber (574.13 – 618.21 cm^{-1}), which is maybe due to the replacement of smaller ionic radius Fe^{3+} ions with the larger ionic radius Zr^{4+} ions [29] is shown in Fig. 2b. Thus it again confirms the incorporation of Zr^{4+} ions into the $CuFe_2O_4$ crystal lattice.

UV-DRS Analysis

Figure 3a shows the optical absorption spectrum of all the synthesized samples which is recorded between the wavelength from 200—900 nm. From the spectrum, it is noted that the absorption range is slightly shifted towards the blue end of the spectrum. Hence it confirms that the bandgap of the material is increased with the addition of Zr^{4+} ions into the $CuFe_2O_4$ crystal lattice. The optical bandgap of the material is calculated using Tauc's relation (Eq. 4) and the corresponding plot is shown in Fig. 3b.

$$\alpha h\nu = A\left(h\nu - E_g\right)^{1/2} \tag{4}$$

The calculated band gap values are 1.39 eV, 1.56 eV, 1.80 eV, and 1.97 eV for S1, S2, S3, and S4 samples respectively. This increase in optical bandgap energy with respect to Zr concentration is may be due to the formation

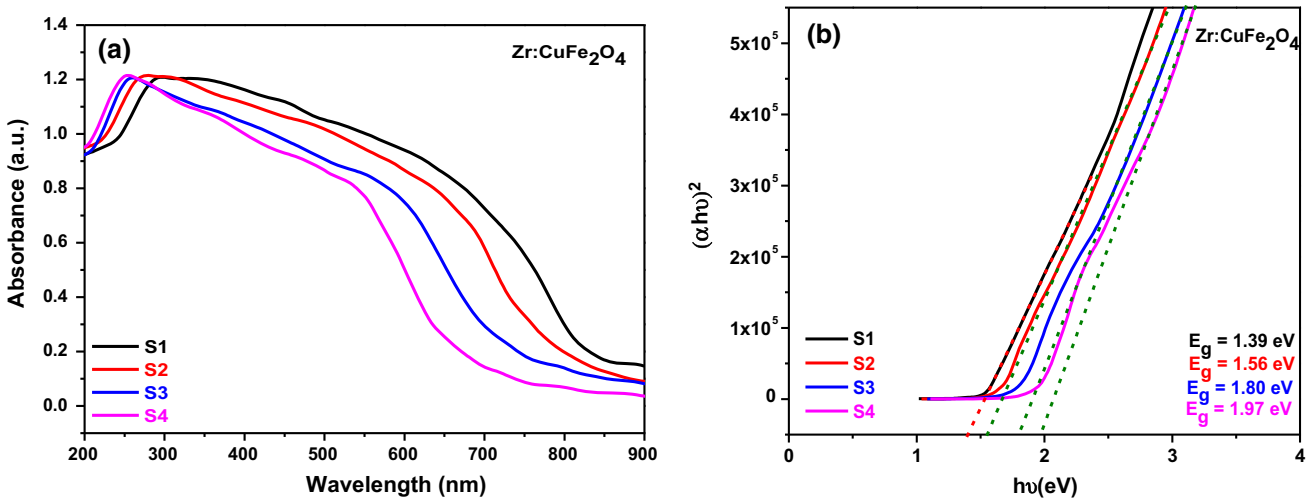

Fig. 3 **a** UV-DRS absorption spectra of the prepared materials. **b** Tauc's plot of the prepared materials

of sub-band energy level and defects in the crystal lattices [30, 31]. Also, the obtained bandgap for pure copper ferrite (S1) is quietly matched with the previous reports [32, 33].

Photoluminescence (PL) Analysis

Figure 4, illustrates the room temperature PL spectrum of all the prepared nanomaterials recorded between the wavelength range 325 – 700 nm with an excitation wavelength of 320 nm. All the four prepared samples exhibit a strong emission in the UV region (Near Band Emission) around 368 nm is related to the radiative recombination that occurs by surface electrons of the materials [34]. The emission in the green region (540 nm), and orange-red region (640 nm) is owing to the radiative transition of electrons from swallow donors which is trapped by the Zr^{4+} sub energy levels, interstitial and singly ionized oxygen vacancies [35]. In addition, it is noted that the NBE is slightly shifts towards the lower wavelength is because of the slight increase in the bandgap of the materials with the increase of Zr^{4+} content. Also, the near band emission is high than that of the deep-level emission confirms the good crystalline nature of all the prepared materials [36]. The deep level emission in the spectrum reveals that the synthesized materials exhibit defects and thus it helps to improve the photocatalytic behavior of the catalyst material.

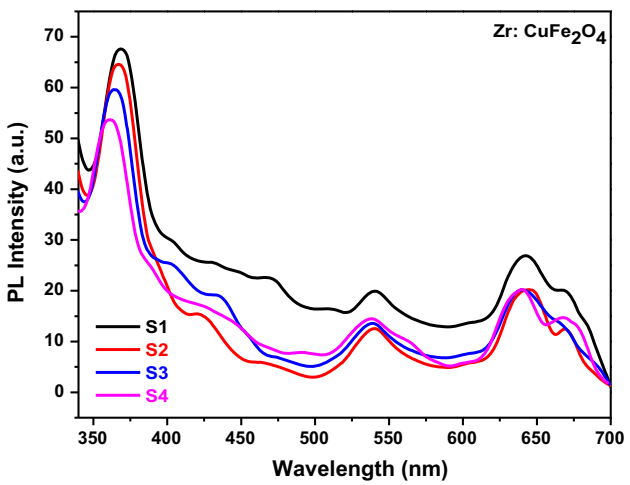

Fig. 4 PL spectra of the prepared samples

SEM and EDAX Analysis

The morphology of the synthesized samples is studied by scanning electron microscope instruments. Figure 5a–d illustrates the SEM images of the S1, S2, S3, and S4 samples respectively with the magnification of 2 μm range. From the images, it is observed that the pure $CuFe_2O_4$ sample not having the specific morphology and it looks like an agglomerated cluster of particles, whereas the morphology has improved to a regular pattern as the Zr^{4+} content is increases and finally attains wheat like morphology for 5 wt% of Zr^{4+} doped $CuFe_2O_4$ sample (S4). Figure 5 (e, f, g, h) shows the EDAX spectrum of S1, S2, S3, and S4 samples respectively. The EDAX spectrum consists of corresponding peaks for Cu, Fe, O, and Zr ions and it confirms the presence of those ions in the prepared samples and also there were no impurity peaks were found in the spectrum reveals the purity of the synthesized material.

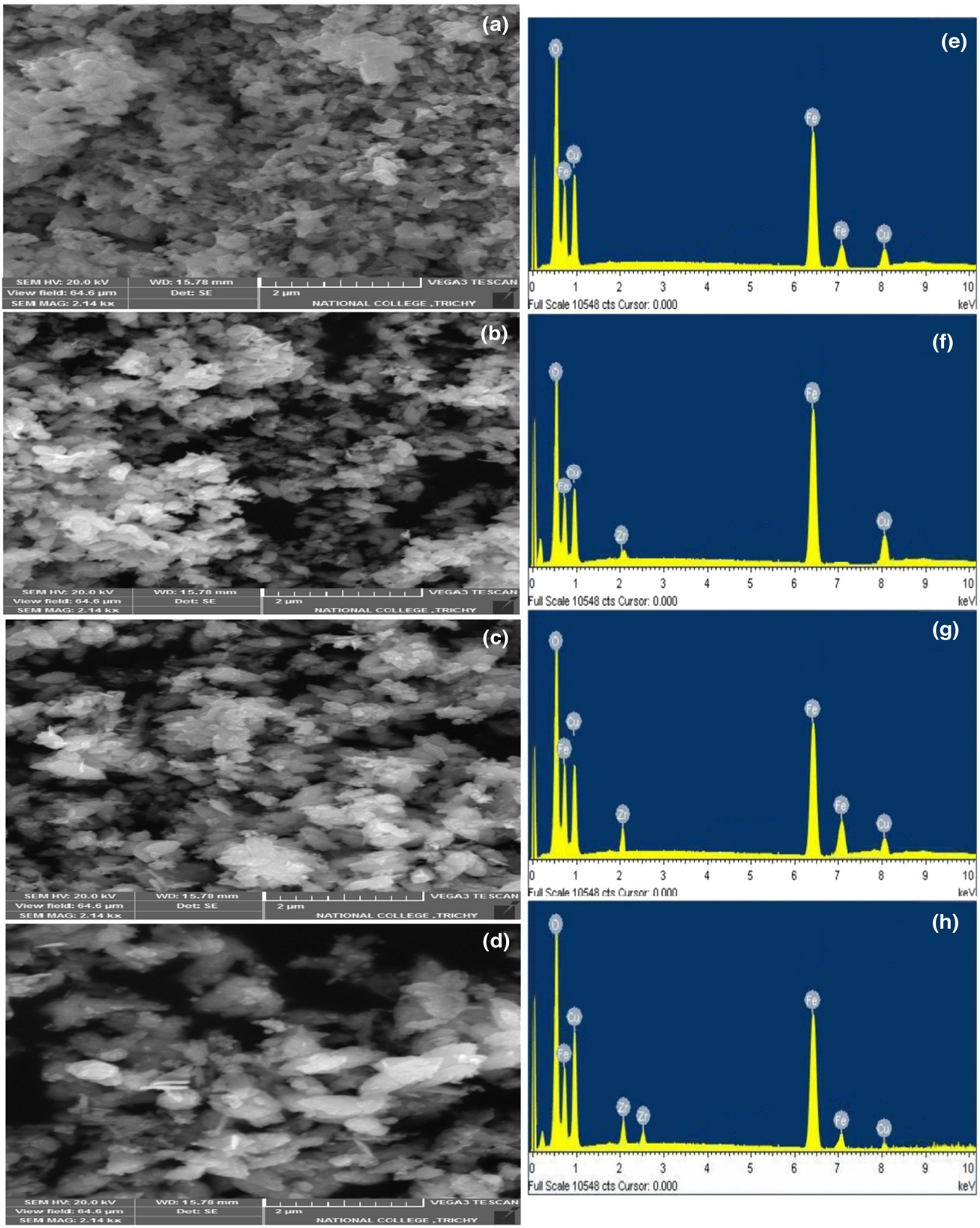

Fig. 5 **a**, **b**, **c**, **d** SEM micrographs of the prepared samples, and **e**, **f**, **g**, **h** EDAX spectrum of the prepared samples

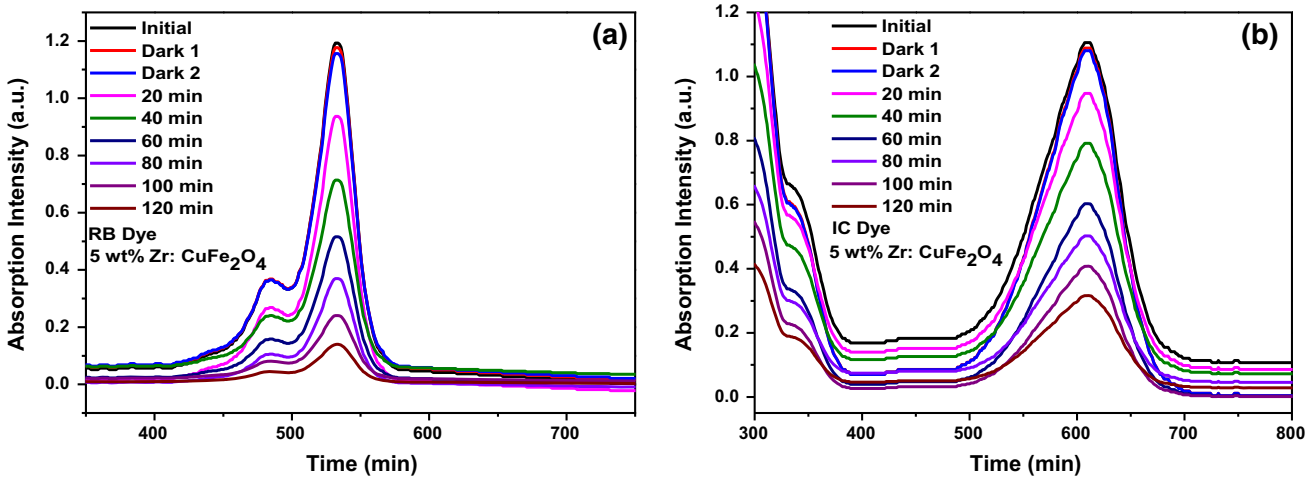

Fig. 6 **a**, **b** UV absorption spectra of RB and IC dye loaded with 5wt% of Zr doped $CuFe_2O_4$ NPs

Photocatalytic Experiment

The degradation UV spectrum of the 5 wt% Zr doped $CuFe_2O_4$ catalyst loaded RB and IC dyes were shown in Fig. 6a, b respectively. From the spectrum, the maximum absorption intensity peaks are observed at 533 nm and 609 nm respectively for RB and IC dyes and gradually decrease as a function of reaction time. Hence, the degradation of dye molecules is confirmed by these phenomena. The C/C_0 was calculated for each time interval and a graph was comparatively drawn between consecutive C/C_0 values with respective reaction time intervals for all the samples S1, S2, S3, and S4 to estimate the degradation percentage of the dye molecules and is shown for RB and IC dyes respectively in Fig. 7a, b. The degradation efficiency is calculated as 40%, 58%, 71%, 88% for S1, S2, S3, and S4 with RB dye and 35%, 46%, 55%, 71% for S1, S2, S3, and S4 with IC dye within 120 min. From the degradation phenomena, it is confirmed that the reaction follows the pseudo-first-order kinetics and the rate constant for the degradation reaction was calculated using Langmuir–Hinshelwood relation (Eq. 5) and by plotting a graph between ln (C/C_0) and their respective reaction time is shown for RB and IC dyes respectively in Fig. 7c, d.

$$\ln\left(\frac{c}{c_0}\right) = kt \tag{5}$$

In general, the photocatalytic reaction involving the heterogeneous nano photocatalyst is wok under the basic principle, that when the light hits the semiconductor nano photocatalyst material the photon energy equal to that of the bandgap energy of the material is absorbed by the electrons in the valence band (VB) of the atoms and excited to the conduction band (CB). Therefore electron–hole separation is created in the photocatalyst material. These electrons in the CB now react with reactive oxygen species in the dye solution and forms superoxide anions (O_2^-). On the other hand, the holes in the VB is reacts with H_2O in the dye solution which in turn forms (•OH) radicals. Now, these created (•OH) radicals and superoxide anions (O_2^-) are reacts with the dye molecules and the mineralization occurs. These overall reactions are collectively called as advanced oxidation process (AOP). In this case, the photo-Fenton reaction is maybe occurred by chance, due to the presence of ferrites (Fe^{3+}) functional group in the prepared materials. From all the above-observed results it was noted that the degradation percentage is improved with the addition of Zr^{4+} content into the $CuFe_2O_4$ nanoparticles. Also, the highest degradation percentage was achieved by 5wt% of Zr^{4+} doped $CuFe_2O_4$ nanoparticles for both dyes RB and IC. This may be due to the slight increase in the bandgap of the material when compared to other prepared materials, such that the excited electron can able to stay in the CB for a while and is easily react with dye solution. Further, the PL intensity of the material is decreased with the increase in Zr^{4+} content. Hence it confirms the electron–hole recombination is prevented by the introduction of Zr^{4+} into the crystal lattice. This is one of the reasons for the gradual increase of photocatalytic performance as a function of Zr^{4+} ions in the prepared materials. Further, the introduction of Zr^{4+} cation into the $CuFe_2O_4$ will provide electron trapping energy level in the crystal and it will improve the photocatalytic activity of the material. In fact, due to an increase in the Zr content in the material, the electron transfer between the $CuFe_2O_4$ and Zr^{4+} is increased. This is because excess electrons will be trapped by Zr^{4+} converting it into Zr^{3+} on continuation the Zr^{3+} will lose the electron to the molecular oxygen and produce $O_2^{\bullet\,-}$ and Zr^{4+} again. Hence, it improves the reactive radical formation and thus degrades the dye solution faster.

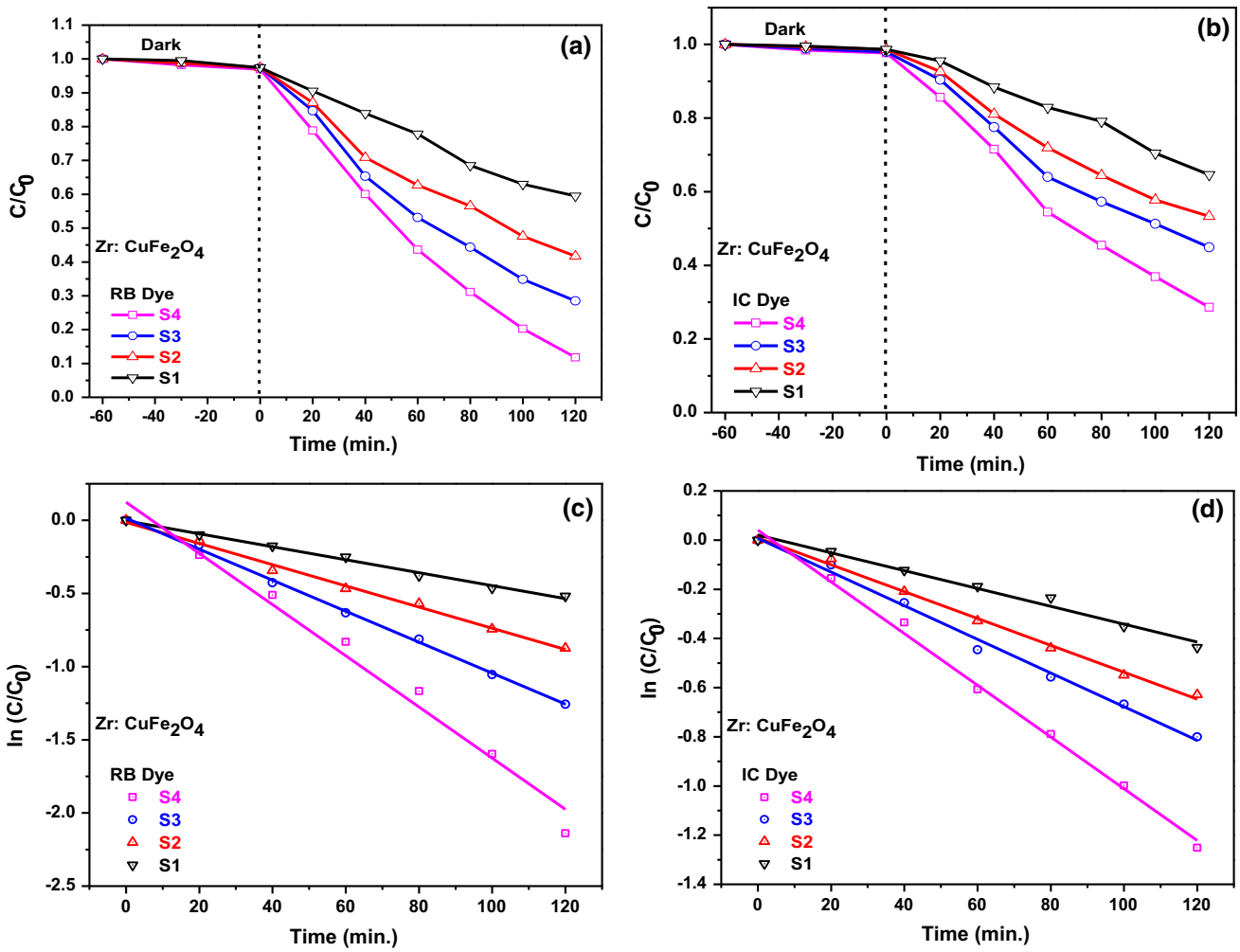

Fig. 7 **a**, **b** Change in concentration (C/C_0) Vs irradiation time for RB and IC dye. **c**, **d** Rate constant for RB and IC dye

Hence, the increase of Zr^{4+} content will increase the photocatalytic performance of the material, so the 5wt% of Zr^{4+} doped $CuFe_2O_4$ nanoparticles have to show maximum efficiency than the other prepared samples. The calculated degradation percentage, rate constant and R^2 values for samples S1, S2, S3, and S4 with RB and IC dyes are tabulated in Table 1. The schematic representation of the energy level diagram is shown in Fig. 8. Some of the previously reported $CuFe_2O_4$ based nanoparticles for photocatalytic applications are tabulated in Table 2, to establish the quality of the present work.

Reaction mechanism

$$Zr^{4+} : CuFe_2O_4 + h\nu \rightarrow h^+_{(vb)} + e^-_{(cb)}$$
$$Zr^{4+} + e^- \rightarrow Zr^{3+}$$
$$Zr^{3+} + O_2 \rightarrow O_2^{\bullet -} + Zr^{4+}$$
$$O_2 + e^- \rightarrow O_2^{\bullet -}(\text{super oxide anions})$$
$$O_2^{\bullet -} + H_2O \rightarrow HO_2^{\bullet} + OH^{\bullet}$$
$$2HO_2^{\bullet} \rightarrow H_2O_2 + O_2^{\bullet}$$
$$e^- + O_2 \rightarrow OH^- + OH^{\bullet}$$
$$e^- + H_2O_2 \rightarrow OH^- + OH^{\bullet}$$
$$h^+ + OH^- \rightarrow OH^{\bullet}$$
$$h^+ + H_2O \rightarrow H^+ + OH^{\bullet}$$
$$OH^{\bullet} + \text{Dye} \rightarrow H_2O + \text{Mineralized products} + CO_2$$
$$O_2^{\bullet -} + \text{Dye} \rightarrow H_2O + \text{Mineralized products} + CO_2$$

Evaluation of Dye Solution Mineralization Using

Table 1 Degradation efficiency and rate constant of the prepared samples for RB and IC dyes

Materials	Dye used	Photocatalytic activity		
		R^2 value	Rate constant (k) ($\times 10^{-3}$ s^{-1})	Degradation percentage (%)
0 wt% Zr:$CuFe_2O_4$ (S1)	RB	0.99261	4.44	40
	IC	0.98127	3.62	35
1 wt% Zr:$CuFe_2O_4$ (S2)	RB	0.99337	7.25	58
	IC	0.9952	5.47	46
3 wt% Zr:$CuFe_2O_4$ (S3)	RB	0.99801	10.59	71
	IC	0.99223	6.85	55
5 wt% Zr:$CuFe_2O_4$ (S4)	RB	0.97651	17.49	88
	IC	0.99476	10.52	71

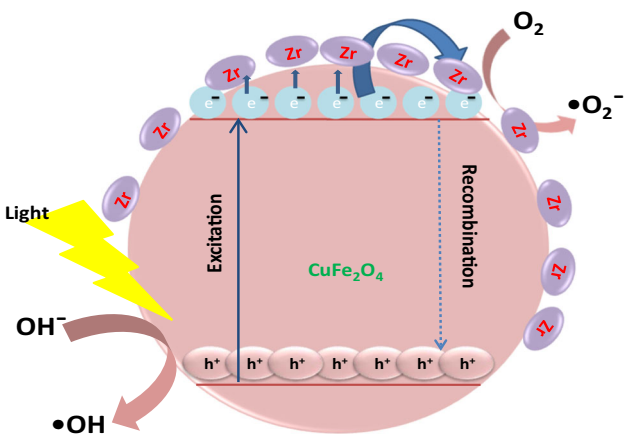

Fig. 8 Energy level diagram of synthesized nanoparticles

Chemical Oxygen Demand (COD) Technique

The chemical oxygen demand (COD) method is one of the simplest and effective routes and is commonly employed to evaluate the organic intensity of wastewater. The analysis helps to measure the contaminant in terms of the overall amount of oxygen available to convert organic compounds to Carbon dioxide and water. In this route, COD was calculated before and after treatment for the dye solution. The loss of COD quantities suggests the dye molecule's mineralization as well as color elimination of the treated dye solution. Here the titration procedure was used to calculate the chemical oxygen deficiency (COD) for the mineralization of the contaminants [41]. Titrations were carried out with ferrous ammonium sulfate (FAS) towards pure

Table 2 Photocatalytic activity of $CuFe_2O_4$ photocatalyst based previously reported works

Materials	Dyes	Percentage of degradation	Reaction time	Light source	Reference
$CuFe_2O_4$	Methylene Blue	94%	105 (min.)	125 W Hg lamp (UV light)	[37]
	Drimarene Yellow	29%	120 (min.)		
$CuFe_2O_4$	Methylene Blue	(With Peroxy di-sulphate PDS) – 94%	75 (min.)	150 W Tungsten halogen lamp (Visible light)	[38]
Zn:$CuFe_2O_4$	Direct Red 264	55%	120 (min.)	Xenon lamp (Visible light)	[22]
Ag:$CuFe_2O_4$	Malachite Green	98%	240 (min.)	UV light	[23]
Ti:$CuFe_2O_4$	Methylene Blue	82%	180 (min.)	500 W Xenon lamp (Visible light)	[24]
$CuFe_2O_4$ / Bi_2O_3	Methylene Blue	90% (With H_2O_2)	45 (min.)	Sodium lamp (Visible light)	[39]
	Acid Scarlet 3R	38%	35 (min.)		
	Rhodamine B	78%	35 (min.)		
$CuFe_2O_4$ / rGO	Phenol	90%	180 (min.)	400 W Xenon lamp (Visible light)	[40]
Zr:$CuFe_2O_4$	Rose Bengal	88%	120 (min.)	150 W Tungsten halogen lamp (Visible light)	Present work
	Indigo Carmine	71%	120 (min.)		

DD water, dye solution after degradation and dye solution before degradation was performed to calculate COD, and the results were computed using the equation below (Eq. 6).

$$COD = \frac{(Blank\ titrate\ value - Dye\ solution\ titrate\ value) \times Normality\ of\ FAS \times 8 \times 1000}{Volume\ of\ the\ solution}\ (ppm) \quad (6)$$

$$\eta = \frac{Initial_{COD} - Final_{COD}}{Initial_{COD}} \times 100(\%) \quad (7)$$

The COD values in percentage for treated RB and IC dye solutions are calculated using Eq. (7) and described in Table 3. In the current analysis, the COD removal efficiency for the RB dyes and IC had reached up to 81% and 74% respectively. Also, COD was measured for the degraded RB and IC dye solutions treated with S1, S2, and S3 samples over the same duration of time, and are observed to be 42%, 58%, 72%, and 39%, 52%, 66%, respectively.

Conclusion

In today's situation, water gets polluted due to the huge development of industrialization and rapid urbanization. So it is necessary to purify the water from the textile industries before it reaches the environmental water sources. In this regard, the zirconium doped copper ferrite nanoparticles were prepared successfully as a suitable photocatalyst through the chemical precipitation method. The structure, crystal phase, morphology, and optical properties were studied using XRD, SEM, DRS and PL characterization techniques. Further, the photocatalytic properties are studied using RB and IC textile dyes for all the prepared materials. The degradation efficiency is calculated as 40%, 58%, 71%, 88% for S1, S2, S3, and S4 with RB dye and 35%, 46%, 55%, 71% for S1, S2, S3, and S4 with IC dye. From the results, the maximum efficiency was observed for 5wt% of Zr^{4+} doped $CuFe_2O_4$ nanoparticles. Also, the mineralization experiment was carried using the COD method and the maximum mineralization was achieved for 5wt% of Zr^{4+} doped $CuFe_2O_4$ nanoparticles in both RB and IC dyes. This proves that the impregnation of zirconium ions will improve the photocatalytic behavior of the material. Further, from all the above-observed results we conclude that the prepared Zr doped $CuFe_2O_4$ nanoparticles are suitable for environmental wastewater remediation under visible light irradiation.

Table 3 COD removal efficiency of the prepared samples over RB and IC dyes

Material	COD Removal efficiency (%)	
	Rose Bengal (RB)	Indigo Carmine (IC)
0 wt% Zr:$CuFe_2O_4$ (S1)	42	39
1 wt% Zr:$CuFe_2O_4$ (S2)	58	52
3 wt% Zr:$CuFe_2O_4$ (S3)	72	66
5 wt% Zr:$CuFe_2O_4$ (S4)	81	74

References

1. P. C. Vandevivere, R. Bianchi, and W. Verstraete (1998). Treatment and reuse of wastewater from the textile wet-processing industry: review of emerging technologies. *J. Chem. Technol. Biotechnol.* **72** (4), 289–302.
2. J. C. Sin and S. M. Lam (2016). Hydrothermal synthesis of europium-doped flower-like ZnO hierarchical structures with enhanced sunlight photocatalytic degradation of phenol. *Mater. Lett.* **182**, 223–226.
3. R. A. Khataee, A. Karimi, R. D. C. Soltani, M. Safarpour, Y. Hanifehpour, and S. W. Joo (2014). Europium-doped ZnO as a visible light responsive nanocatalyst: Sonochemical synthesis, characterization and response surface modeling of photocatalytic process. *Appl. Catal. A-Gen* **488**, 160–170.
4. V. Augugliaro, C. Baiocchi, A. B. Prevot, E. Grací-López-López, V. Loddo, S. Malato, and E. Pramauro (2002). Azo-dyes photocatalytic degradation in aqueous suspension of TiO_2 under solar irradiation. *Chemosphere* **49** (10), 1223–1230.
5. J. Li and P. L. Bishop (2002). In situ identification of azo dye inhibition effects on nitrifying biofilms using microelectrodes. *Water Sci. Technol.* **46** (1–2), 207–214.
6. F. M. Drumond Chequer, V. D. P. Venancio, M. D. L. P. Bianchi, and L. M. Greggi Antunes (2012). Genotoxic and mutagenic effects of erythrosine B, a xanthene food dye, on HepG2 cells. *Food Chem. Toxicol.* **50** (10), 3447.
7. J. L. Kambey, A. P. Farrell, and L. I. Bendell-Young (2001). Influence of illegal gold mining on mercury levels in fish of North Sulawesi's Minahasa Peninsula, (Indonesia). *Environ. Pollut.* **114** (3), 299–302.
8. S. Panigrahi (1993). Bioassay of mycotoxins using terrestrial and aquatic, animal and plant species. *Food Chem. Toxicol.* **31** (10), 767–790.
9. P. Mpountoukas, A. Pantazaki, E. Kostareli, P. Christodoulou, D. Kareli, S. Poliliou, and T. Lialiaris (2010). Cytogenetic evaluation and DNA interaction studies of the food colorants amaranth, erythrosine and tartrazine. *Food Chem. Toxicol.* **48** (10), 2934–2944.

10. E. E. Ritchie, J. I. Princz, P. Y. Robidoux, and R. P. Scroggins (2013). Ecotoxicity of xanthene dyes and a non-chlorinated bisphenol in soil. *Chemosphere* **90** (7), 2129–2135.
11. J. Naitoh and B. M. Fox (1994). Severe hypotension, bronchospasm, and urticaria from intravenous indigo carmine. *Urology* **44** (2), 271–272.
12. K. A. Giri, T. S. Banerjee, G. Talukder, and A. Sharma (1986). Effects of dyes (indigo carmine, metanil yellow, fast green FCF) and nitrite in vivo on bone marrow chromosomes of mice. *Cancer letters* **30** (3), 315–320.
13. J. Yang, T. G. Monk, and P. F. White (1991). Acute hemodynamic effects of indigo carmine in the presence of compromised cardiac function. *J. Clin. Anesth.* **3** (4), 320–323.
14. Y. Long, Y. Lu, Y. Huang, Y. Peng, Y. Lu, S. Z. Kang, and J. Mu (2009). Effect of C_{60} on the photocatalytic activity of TiO_2 nanorods. *J. Phys. Chem. C* **113** (31), 13899–13905.
15. G. Nagaraju, G. C. Shivaraju, G. Banuprakash, and D. Rangappa (2017). Photocatalytic activity of ZnO nanoparticles: synthesis via solution combustion method. *Mater. Today: Proceed.* **4** (11), 11700–11705.
16. V. V. Kumar, K. Gayathri, and S. P. Anthony (2016). Synthesis of α-MoO_3 nanoplates using organic aliphatic acids and investigation of sunlight enhanced photodegradation of organic dyes. *Mater. Res. Bull.* **76**, 147–154.
17. S. M. Botsa, R. Dharmasoth, and K. Basavaiah (2018). Sonochemical assisted synthesis of CuO for degradation of nitrobenzene under visible light irradiation and antimicrobial activity. *J. Nanosci. Technol.* **4** (5), 467–470.
18. W. Konicki, D. Sibera, E. Mijowska, Z. Lendzion-Bielun, and U. Narkiewicz (2013). Equilibrium and kinetic studies on acid dye Acid Red 88 adsorption by magnetic $ZnFe_2O_4$ spinel ferrite nanoparticles. *J. Colloid Interface Sci.* **398**, 152–160.
19. S. Singhal, R. Sharma, C. Singh, and S. Bansal (2013). Enhanced photocatalytic degradation of methylene blue using $ZnFe_2O_4$ / MWCNT composite synthesized by hydrothermal method. *Indian J. Mater. Sci.* **2013**, 6.
20. M. M. Rashad, R. M. Mohamed, M. A. Ibrahim, L. F. M. Ismail, and E. A. Abdel-Aal (2012). Magnetic and catalytic properties of cubic copper ferrite nanopowders synthesized from secondary resources. *Adv. Powder Technol.* **23**, 315–323.
21. K. Vanheusden, W. L. Warren, J. A. Voigt, C. H. Seager, and D. R. Tallant (1995). Impact of Pb doping on the optical and electronic properties of ZnO powders. *Appl. Phys. Lett.* **67** (9), 1280–1282.
22. M. KamelAttarKar, R. Fazaeli, F. Manteghi, and M. Ghahari (2019). Structural, optical, and isothermic studies of $CuFe_2O_4$ and Zn-doped $CuFe_2O_4$ nano ferrite as a magnetic catalyst for photocatalytic degradation of direct red 264 under visible light irradiation. *Environ. Prog. Sustain. Energy* **38** (4), 13109.
23. B. S. Surendra (2018). Green engineered synthesis of Ag-doped $CuFe_2O_4$: Characterization, cyclic voltammetry and photocatalytic studies. *J. Sci-Adv. Mater. Dev.* **3** (1), 44–50.
24. M. N. Arifin, K. M. R. Karim, H. Abdullah, and M. R. Khan (2019). Synthesis of titania doped copper ferrite photocatalyst and its photo activity towards methylene blue degradation under visible light irradiation. *Bull. Chem. React. Eng. Catal.* **14** (1), 219.
25. K. Elayakumar, A. Manikandan, A. Dinesh, K. Thanrasu, K. K. Raja, R. T. Kumar, and A. Baykal (2019). Enhanced magnetic property and antibacterial biomedical activity of Ce^{3+} doped $CuFe_2O_4$ spinel nanoparticles synthesized by sol-gel method. *J. Magn. Magn. Mater.* **478**, 140–147.
26. V. Manikandan, A. Vanitha, E. R. Kumar, and J. Chandrasekaran (2017). Effect of In substitution on structural, dielectric and magnetic properties of $CuFe_2O_4$ nanoparticles. *J. Magn. Magn. Mater.* **432**, 477–483.
27. M. A. Haija, G. Basina, F. Banat, and A. I. Ayesh (2019). Adsorption and gas sensing properties of $CuFe_2O_4$ nanoparticles. *Mater. Sci-Poland* **37** (2), 289–295.
28. M. H. Habibi and H. J. Parhizkar (2014). FTIR and UV–vis diffuse reflectance spectroscopy studies of the wet chemical (WC) route synthesized nano-structure $CoFe_2O_4$ from $CoCl_2$ and $FeCl_3$. *Spectrochim. Acta A: Mol. Biomol. Spectrosc.* **127**, 102–106.
29. M. A. El-Sayed (2002). Influence of zinc content on some properties of Ni–Zn ferrites. *Ceram. Int.* **28** (4), 363–367.
30. A. Singh, S. Jauhar, V. Kumar, J. Singh, and S. Singhal (2015). Synthesis of zinc substituted cobalt ferrites via reverse micelle technique involving in situ template formation: a study on their structural, magnetic, optical and catalytic properties. *Mater. Chem. Phys.* **156**, 188–197.
31. A. Singh, A. Goyal, and S. Singhal (2014). Nickel-doped cobalt ferrite nanoparticles: efficient catalysts for the reduction of nitro aromatic compounds and photo-oxidative degradation of toxic dyes. *Nanoscale* **6** (14), 7959–7970.
32. N. Kezzim, A. Abdi. Nasrallah, and M. Trari (2011). Visible light induced hydrogen on the novel hetero-system $CuFe_2O_4/TiO_2$. *Energy Convers. Manag.* **52** (8–9), 2800–2806.
33. S. Sakthi. Karunakaran, P. Gomathisankar. Raadha, and P. Vinayagamoorthy (2013). Nanostructures and optical, electrical, magnetic, and photocatalytic properties of hydrothermally and sono-chemically prepared $CuFe_2O_4/SnO_2$. *RSC Adv.* **3** (37), 16728–16738.
34. X. L. Wu, G. G. Siu, C. L. Fu, and H. C. Ong (2001). Photoluminescence and cathode-luminescence studies of stoichiometric and oxygen-deficient ZnO films. *Appl. Phys. Lett.* **78** (16), 2285–2287.
35. Z. L. Wang (2004). Zinc oxide nanostructures: growth, properties and applications. *J. Phys. Condens. Matter* **16** (25), R829.
36. S. Gnanam and V. Rajendran (2013). Facile hydrothermal synthesis of alpha manganese sesquioxide (α-Mn_2O_3) nanodumbbells: structural, magnetic, optical and photocatalytic properties. *J. Alloys Compd.* **550**, 463–470.
37. M. S. Amulya, H. P. Nagaswarupa, M. A. Kumar, C. R. Ravikumar, K. B. Kusuma, and S. C. Prashantha (2021). Evaluation of bifunctional applications of $CuFe_2O_4$ nanoparticles synthesized by a sonochemical method. *J. Phys. Chem. Solids* **148**, 109756.
38. S. Anandan, T. Selvamani, G. G. Prasad, A. M. Asiri, and J. J. Wu (2017). Magnetic and catalytic properties of inverse spinel $CuFe_2O_4$ nanoparticles. *J. Magn. Magn. Mater.* **432**, 437–443.
39. S. Munir, A. Rasheed, S. Zulfiqar, M. Aadil, P. O. Agboola, I. Shakir, and M. F. Warsi (2020). Synthesis, characterization and photocatalytic parameters investigation of a new $CuFe_2O_4/Bi_2O_3$ nanocomposite. *Ceram. Int.* **46** (18), 29182–29190.
40. M. A. Othman, I. Haija, J. H. Ismail, and F. Zain (2019). Preparation and catalytic performance of $CuFe_2O_4$ nanoparticles supported on reduced graphene oxide ($CuFe_2O_4$/rGO) for phenol degradation. *Mater. Chem. Phys* **238**, 121931.
41. K. Ravichandran, K. S. Seelan, P. Kavitha, and S. Sriram (2019). Influence of Cu+ g-C_3N_4 incorporation on the photocatalytic dye decomposition of ZnO film coated on stainless steel wire meshes. *J. Mater. Sci. Mater. Electron* **30** (22), 19703–19717.

Publisher's Note Springer Nature remains neutral with regard to jurisdictional claims in published maps and institutional affiliations.